

Observations and Analysis of the Non-Radial Propagation of Coronal Mass Ejections Near the Sun

Paulett Liewer¹ · Olga Panasenco² · Angelos Vourlidas³ ·
Robin Colaninno⁴

Received: 2 April 2015 / Accepted: 28 September 2015 / Published online: 29 October 2015
© Springer Science+Business Media Dordrecht 2015

Abstract The trajectories of coronal mass ejection (CME) are often observed to deviate from radial propagation from the source while within the coronagraph field of view ($R < 15 - 30 R_{\text{sun}}$). To better understand nonradial propagation within the corona, we first analyze the trajectories of five CMEs for which both the source and 3D trajectory (latitude, longitude, and velocity) can be well determined from solar imaging observations, primarily using observations from the twin *Solar TErrestrial RElations Observatory* (STEREO) spacecraft. Next we analyze the cause of any nonradial propagation using a potential field source surface (PFSS) model to determine the direction of the magnetic pressure forces exerted on the CME at various heights in the corona. In two cases, we find that the CME deviation from radial propagation primarily occurs before it reaches the coronagraph field of view (below 1.5 solar radii). Based on the observations and the magnetic pressure forces calculated from the PFSS model, we conclude that for these cases the deviation is the result of strong active-region fields causing an initial asymmetric expansion of the CME that gives rise to the apparent rapid deflection and nonradial propagation from the source. Within the limitations of the PFSS model, the magnetic fields for all five cases appear to guide the CMEs out of the corona through the weak-field region around the heliospheric current sheet even when the current sheet is inclined and warped.

Keywords Corona mass ejections · Corona · Space weather

Electronic supplementary material The online version of this article (doi:[10.1007/s11207-015-0794-9](https://doi.org/10.1007/s11207-015-0794-9)) contains supplementary material, which is available to authorized users.

✉ P. Liewer
Paulett.Liewer@jpl.nasa.gov

¹ Jet Propulsion Laboratory, California Institute of Technology, Pasadena, CA 91109, USA

² Advanced HelioPhysics, Pasadena, CA 91106, USA

³ Applied Physics Laboratory, The Johns Hopkins University, Laurel, MD 20723, USA

⁴ Naval Research Laboratory, Space Science Division, Washington, DC 20375, USA

1. Introduction

Observations made with the earliest coronagraphs showed that the trajectories of coronal mass ejections (CMEs) were often deflected within the field of view (FOV) of the coronagraphs. During periods of low solar activity, CMEs were observed to be deflected toward the streamer belt, suggesting that the deflection was controlled by the overall flow and magnetic field configuration of the corona (MacQueen, Hundhausen, and Conover, 1986; Hundhausen, 1993). The early coronagraph images also showed that CME position angles (the CME centroid angle as measured counterclockwise from solar north) were confined to equatorial regions at solar minimum, but were spread out over all position angles at solar maximum (Howard *et al.*, 1985 and references therein). The advent of the *SOlar and Heliospheric Observatory* (SOHO) with its three coronagraphs and extreme-ultraviolet telescope led to a dramatic increase in our understanding of the solar sources of CMEs (see, *e.g.*, Plunkett *et al.*, 2001). These images showed that at solar minimum, most CMEs originate near the solar equator, but CMEs starting from higher latitudes were often deflected toward the equatorial regions (Schwenn, 2000).

Cremades and Bothmer (2004) analyzed the deviation of CME position angles from their source region latitudes for 124 “structured” SOHO CMEs, which were well observed by the *Extreme Ultraviolet Telescope* (EIT) and by the *Large Angle and Spectroscopic Coronagraph* (LASCO). They found a “pronounced and systematic confinement” of the CME position angles to solar equatorial position angles and equatorward deviations during low solar activity (1996 to mid-1998). In contrast, at times of high activity, the deviations of the position angle from the source latitude fluctuated strongly either toward the poles or the equator without a systematic trend. These results were consistent with those from earlier coronagraph observations, but the latitudes of the sources were now determined from the EIT observations, and the deviations from the source latitude could be quantified. Cremades, Bothmer, and Tripathi (2006) estimated the influence of coronal holes on the CME trajectory using a “*fictitious force*” that depended on the area of and the distance to the hole. A good correlation was found between the measured deviation and the sum of the fictitious forces from all holes, including the large polar coronal holes. These results indicated that the coronal magnetic fields were the cause of the observed deviations. The calculation was only applied to the N–S component since only the deviation in position angle was known. It is important to realize that the position angle, as measured in the LASCO images, is a projection of the actual propagation vector onto the plane of the sky and is always greater than the true propagation latitude. Gopalswamy *et al.* (2009) used a similar calculation of a fictitious force to analyze the influence of coronal holes on the observed E–W deflection from the radial propagation of six SOHO CMEs. This study, which also included 18 CMEs that were not deflected, confirmed that the deflection was correlated with the fictitious coronal hole force. The authors concluded that the open flux of the coronal holes acted as a “magnetic wall that constrains the CME propagation.”

With the launch of the *Solar TERrestrial RElations Observatory* (STEREO), it became possible to use multiple viewpoints to determine the three-dimensional (3D) trajectories of CMEs. This allows determining the deflection in longitude as well as the true unprojected deviation in latitude from the source location. STEREO’s imaging suite, the *Sun Earth Connection Coronal and Heliospheric Investigation* (SECCHI), consists of an *Extreme Ultra Violet Imager* (EUVI) covering $R < 1.5 R_{\text{sun}}$, two coronagraphs, COR1 ($1.5 R_{\text{sun}} < R < 4.3 R_{\text{sun}}$) and COR2 ($2.5 R_{\text{sun}} < R < 15 R_{\text{sun}}$), and two heliospheric imagers, HI1 and HI2, covering out to 70° elongation from the Sun (Howard *et al.*, 2008).

Using STEREO data and the forward-modeling technique to derive the trajectory of CMEs from the multiple viewpoints (Thernisien, Howard, and Vourlidas, 2006). Kilpua

et al. (2009) analyzed the trajectories out to 1 AU of two CMEs originating at high latitudes. One, a slow CME associated with a polar crown filament eruption, was found to deflect southward toward the solar equator; it was later detected *in situ* at STEREO A. The CME showed a clear asymmetric expansion that indicated the influence of the polar coronal hole fields on the eruption and trajectory of the CME. The authors concluded that the polar coronal hole fields had guided the CME to the equator. The second CME, a fast CME from an active region, did not appear to be deflected and was not detected by any spacecraft (Kilpua *et al.*, 2009).

Byrne *et al.* (2010) also used STEREO observations and a novel stereoscopic fitting technique to reconstruct the curved front of the CME on 2008 December 12 and tracked its expansion and propagation through the corona to 1 AU. They found that the CME was deflected from the polar region toward the equator and compared STEREO observations with the *in situ* ICME observation. As in Kilpua *et al.* (2009), they observed an axisymmetric southward-dominated expansion of the CME; many possible causes of the deflection and expansion were cited. Liu *et al.* (2010a), using a new geometric triangulation technique on STEREO white-light data, tracked the same 2008 December 12 CME from the Sun to 1 AU, also noting its nonradial propagation. Liu *et al.* (2010b) analyzed the propagation of three CMEs, including that analyzed in Liu *et al.* (2010a), using STEREO white-light data starting from the outer coronagraph (COR2). They used the forward-modeling technique of Thernisien, Howard, and Vourlidas (2006) to determine the trajectory near the Sun and the geometric triangulation technique of Liu *et al.* (2010a) to follow the same CME to 1 AU, allowing a firm association between the CME as seen near the Sun and the *in situ* ICME observations. All of the CMEs showed a westward deflection, but it was noted that the value quoted should be considered a lower limit since only data from the outer coronagraph and beyond were used in the analysis.

Shen *et al.* (2011), also using the forward-modeling technique (Thernisien, Howard, and Vourlidas, 2006) to determine the trajectory from multiple viewpoint observations, analyzed the deflection of one CME trajectory through the corona. In addition, they used a potential field source surface (PFSS) model to calculate the magnetic energy density gradient force on the CME at different heights to study the cause of the deflection. They found that the nonuniform distribution of the background magnetic field energy density influenced the trajectory at early stages and that the CME tended to propagate to the region with the lower magnetic energy density, *e.g.*, toward the heliospheric current sheet (HCS). Gui *et al.* (2011) used the same techniques and extended the work of Shen *et al.* (2011). They analyzed the deflection in both latitude and longitude of ten CMEs and found a positive correlation between the deflection rate and the strength of the gradient in the magnetic energy density. This work confirmed the conclusion of Shen *et al.* (2011): the deflections of CMEs are mainly controlled by the background magnetic field, and CMEs tend to deflect toward the region of low magnetic energy density surrounding the HCS.

Magnetohydrodynamic (MHD) simulations, in conjunction with multi-viewpoint observations, have been used with great success to help understand various aspects of CMEs, including nonradial propagation (see review by Lugaz and Roussev, 2011 and reference therein). Lugaz *et al.* (2009) used 3D MHD modeling to analyze the interaction of the two fast CMEs observed by STEREO. Synthetic white-light images created from the MHD model were compared to SECCHI coronagraph and heliospheric imager observations to help interpret the data and understand the interactions of the CMEs with each other and with the corona and the structured solar wind. Both synthetic images and LASCO coronagraph observations showed a deflection of two coronal streamers by the first CME and a distortion of the second CME front as it propagated into the denser plasma of the deflected streamer; the merging occurred in the FOV of the heliospheric imagers (Lugaz *et al.*, 2009).

In a separate study of interacting CMEs, Lugaz *et al.* (2012) used 3D MHD modeling and observations to analyze the propagation and merging of two CMEs tracked by STEREO to 1 AU. By combining the modeling with remote-sensing and *in situ* observations, they concluded that a collision of the CME at about 0.8 AU had led to a deflection of the first CME by about 10° toward the Sun–Earth line. Zuccarello *et al.* (2012) used 2.5D (cylindrical symmetry) MHD modeling and observations to analyze the cause of the 15° deflection in latitude of a CME toward the HCS. They concluded that magnetic fields of the overlying helmet streamer were the key factor that caused the observed deflection; increasing the solar dipole field increased the rate of deflection.

Understanding nonradial propagation is important to improve our ability to forecast whether or not a CME and/or its shock will impact Earth, which has implications for space weather. Knowing the CME trajectory (direction and velocity) as it leaves the corona is especially important for real-time space weather prediction. This near-Sun ($\sim 10\text{--}30 R_{\text{sun}}$) trajectory information from coronagraph observations is frequently used as input for CME propagation models, such as NOAA’s ENLIL (Odstrcil, 2004), which is currently used in operational space-weather forecasting (<http://www.swpc.noaa.gov/products/wsa-enlil-solar-wind-prediction>). Moreover, while the CME front can be distorted by interaction with the solar wind beyond the corona, the momentum of a fast and massive CME (speed $> 500 \text{ km s}^{-1}$ and mass $> 10^{15} \text{ g}$) is too high for its direction to be substantially changed by interaction with the background solar wind.

Following previous multi-viewpoint observational studies of nonradial CME propagation, we here use coronagraph observations to determine the deviation from radial propagation from the source region for five CMEs. The goals of the study are to investigate the roles of both coronal hole and active region fields in nonradial CME propagation and to further investigate whether the observed deviation is toward the HCS during periods of strong solar activity as well as near solar minimum.

We present results from analyzing five CMEs for which the solar source regions are well determined, whose trajectories in 3D can be determined from STEREO coronagraph observations, and that show no evidence of CME–CME interaction. The trajectories are determined by fitting coronagraph observation using the forward-modeling technique of Thernisien, Howard, and Vourlidas (2006). We use the PFSS model of Schrijver and DeRosa (2003) to analyze the coronal magnetic pressure forces acting on the CME at different heights in the corona. We use EUVI data for the first time to analyze the nonradial propagation below the coronagraph FOV in combination with analyzing the magnetic forces at these heights. This led to the conclusion that nonradial propagation can result not only from large-scale coronal fields, but also from initial asymmetric expansion caused by the nearby strong active-region fields. Neighboring active-region fields can cause very rapid (with a few solar radii) asymmetric expansion of the CME, giving rise to apparent deflection and large deviations from radial propagation from the source. Since the PFSS fields beyond the source surface at $2.5 R_{\text{sun}}$ are radial, the location of the PFSS current sheet at $2.5 R_{\text{sun}}$ can also be used to approximate the location of the HCS farther out. We find that within the limitations of the PFSS model, the coronal magnetic fields in these five cases guide the CMEs out through the weak field region around the HCS even when the current sheet is highly inclined and warped. The CME does not follow the shortest path to the HCS; the path depends on the local and global gradients in the magnetic pressure.

The outline of this article is as follows. In Section 2 we describe the observations and analysis method. In Section 3 we report the results of analyzing the five CMEs. Section 4 contains a summary and discussion.

2. Observations and Method of Analysis

To analyze the nonradial propagation of CMEs near the Sun, we first searched for CMEs whose source regions were well determined and which appeared to deviate substantially (10° or more) from radial propagation, based on the change in position angle in one of the STEREO/COR2 images. Large deviations were required because of the relatively large errors in the 3D trajectory determination technique, as described below. We also required that the CME be well observed by both STEREO spacecraft to obtain an accurate 3D trajectory. At periods of high activity, multiple CMEs are often visible in coronagraph images, which makes determining the trajectory difficult; this eliminated many candidates. In addition, because the goal is to study the effects of coronal magnetic fields on the trajectories, we eliminated CMEs that showed evidence of CME–CME interaction in the coronagraph images. These interactions may alter the trajectories and make determining the 3D trajectory difficult. To date, we have found only four events that satisfy all these criteria. In addition, we included one case that met the criteria except that it showed no significant deviation from radial propagation; this CME was analyzed as a check on our method for analyzing the effects of coronal magnetic fields on the trajectories.

The 3D trajectory of each CME was determined using simultaneous multi-viewpoint coronagraph observations of the CME and the graduate cylindrical shell (GCS) forward model to fit the CME geometry and position (Thernisien, Howard, and Vourlidas, 2006; Thernisien, Vourlidas, and Howard, 2009; Thernisien, 2011). Briefly, the method assumes that the CME has a croissant shape approximating a magnetic flux-rope geometry, parameterized as a graduated cylindrical shell; the density is assumed to be concentrated on the surface. The parameters of the model are adjusted by the user to best fit the model to the multiple-viewpoint coronagraph images (STEREO and/or LASCO). During this fitting, the model CME can also be rendered into synthetic coronagraph images using Thomson scattering to improve the fit to the coronagraph images. The errors for this technique are on the order of 5° in latitude and 10° in longitude. The software with instructions is available in the *SolarSoft* tree.

We fit the CME at multiple times to determine the velocity as well as the latitude and longitude of the trajectory. Since we are interested in knowing the trajectory of the CME as it leaves the corona, the trajectory was taken as the value determined from the maximum height fit in the COR2 FOV. No assumption was made about the initial location of the CME near the solar surface when the model was fit to the coronagraph images.

The location of the source region can be determined to a much greater accuracy (within a few degrees) than either the CME trajectory or the location of the HCS. The source location was determined from EUV images using flare ribbons and a post-eruption flare arcade (PEA) from $H\alpha$ images of pre-eruption filaments. When the source location extended over several degrees of longitude and latitude, we used the centroid.

The five cases analyzed, along with the source coordinates and trajectory coordinates and velocity, are listed in Table 1 organized by date. Throughout this article, the source and trajectory are given in Carrington longitude and heliographic latitude, both in degrees. The last two columns give the deviation of the trajectory from radial, that is, the difference between the trajectory's latitude and longitude and those of the source. The first three events are from the set of 24 CMEs analyzed in the study by Möstl *et al.* (2014) of methods for predicting Earth arrival times. Some of these events have been analyzed previously, as noted below.

After we ascertained the deviation (or lack thereof) in the trajectory from radial propagation from the source, we used a PFSS coronal field model to investigate the magnetic

Table 1 CME source locations, trajectories, and deviations from radial propagation.

Event	CME date	Source region		CME trajectory			Deviation (CME-source)	
		Carrington longitude	latitude	Carrington longitude	latitude	velocity (km s ⁻¹)	latitude	longitude
Case 1	2008 December 12	85	50	74	8	497	-42	-11
Case 2	2010 April 03	261	-25	259	-25	829	0	-2
Case 3	2010 April 08	180	24	195	-7	511	-31	15
Case 4	2010 May 1	233	20	207	-8	261	-28	-26
Case 5	2010 August 14	351	13	341	-12	867	-25	-13

pressure force acting on the CME in the corona. The magnetic force on the CME can be written in the form

$$\vec{F} = \frac{\vec{J} \times \vec{B}}{c} = -\nabla \frac{B^2}{8\pi} + \frac{(\vec{B} \cdot \nabla) \vec{B}}{4\pi} = -\nabla_{\perp} \frac{B^2}{8\pi} + \frac{B^2}{4\pi R} \vec{n}.$$

The first term on the far right is the magnetic pressure force, and the second term is the magnetic tension, where \perp is perpendicular to the magnetic field and \vec{n} is parallel. We made contour plots of the magnetic pressure force at various heights above the surface to determine the direction of the magnetic pressure force on the CME. Specifically, we investigated the role of the active-region fields that are evident in contour plots close to the surface ($R < 1.25 R_{\text{sun}}$), and the role of the large-scale fields that dominate the contour plots higher in the corona.

The PFSS models are very much an approximation of the actual coronal fields for several reasons. The model assumes that the corona carries no currents and uses as an inner boundary condition a synoptic scalar magnetogram that is derived from about 26 days of magnetograph data. Moreover, the model assumes that the corona is static. During a CME, the corona is far from static or current-free. Not only the local, but also the larger-scale fields of the corona can be affected by the CME. Coronal streamers are frequently observed to be deflected by CMEs (Subramanian *et al.*, 1999). Because of these limitations, the PFSS contour plots are used only to determine the general direction of the magnetic pressure forces on the CME. We did not attempt to include the influence of magnetic tension forces because the magnetic reconnection accompanying the eruptions presumably causes the tension forces to change rapidly. Kay, Opher, and Evans (2013) have developed a method for predicting CME propagation directions that include both magnetic pressure and magnetic tension forces; they find that the tension forces can be strong. It is also possible that the orientation of the CME magnetic field with respect to the neighboring coronal fields will affect the trajectory of the CME, as seen in the simulations of Zhou and Feng (2013).

The PFSS model was also used to estimate the location of the HCS to ascertain whether the CMEs tend to leave the corona through the weak field region around the HCS. PFSS models solve for the magnetic field in the region between the solar surface and the source surface, usually placed at $2.5 R_{\text{sun}}$; the magnetic field is assumed to be radial beyond this source surface. Thus, in this model, the latitude and longitude of the HCS beyond $2.5 R_{\text{sun}}$ is the same as at the source surface. We chose to use the PFSS model of Schrijver and DeRosa (2003), available in *SolarSoft*, which partially compensates for the fact that traditional synoptic magnetograms use data extending back over one solar rotation. In this model, the magnetic field on the solar surface is evolved in time from the date of the magnetogram

data to the date of the synoptic magnetogram using a flux transport model that includes differential rotation and diffusion.

Coronagraph observations indicate that streamers are generally, but not always, co-located with the HCS as calculated from PFSS models (Liewer *et al.*, 2001 and references therein). The co-location of the streamer belt and HCS was demonstrated by Wang, Sheeley, and Rich (2000), who, using PFSS models with a simple model for the density of the streamer belt, were able to create synthetic coronagraph observations consistent with the coronagraph images. Therefore we also compared the magnetic structure predicted by the PFSS model to the pre-event structure observed by the coronagraph, comparing the predicted location of the HCS and the observed location of the streamer belt as a check on the PFSS model. We note, however, that the visibility of the streamer belt in a coronagraph image depends on the inclination of the current sheet in the plane of sky (Wang, Sheeley, and Rich, 2000). The intensity in the coronagraph image depends directly on the integrated line-of-sight density, and thus a streamer belt that is nearly vertical in the coronagraph plane of sky may be very faint in the image, whereas a flat, horizontal streamer belt will be quite bright. Of course, for complex solar magnetic fields such as during solar maximum, there can also be coronal streamers, such as pseudostreamers, that do not coincide with the main HCS streamer belt.

3. Results

3.1. Case 1: CME on 2008 December 12

The CME on 2008 December 12 is associated with a polar crown filament eruption occurring at approximately 3 UT. As discussed in the introduction, the nonradial propagation of this CME has been studied previously using multi-viewpoint data (Byrne *et al.*, 2010; Liu *et al.*, 2010a, 2010b). These previous works mainly focused on tracking the CME to 1 AU and on comparing it with the *in situ* ICME data; the cause of the nonradial propagation was not analyzed. Panasenco *et al.* (2011, 2013) analyzed the associated nonradial prominence eruption and showed that the prominence and CME follow different trajectories early in the eruption. Various other aspects of this event have also been studied. For example, DeForest, Howard, and McComas (2013), using both STEREO/SECCHI and L1 data, studied the morphology of this CME and identified features (cavity, sheath, etc.) seen in EUV and white light with those seen *in situ*. This CME was also one of the events analyzed by Gui *et al.* (2011), who used methods very similar to ours to determine the extent and cause of the nonradial propagation. We include this case in our study as a comparison with previous work and add a more detailed analysis of the magnetic pressure gradients around the pre-eruptive filament and their influence on the trajectory.

The CME is first seen in COR1 difference movies (<http://cor1.gsfc.nasa.gov/dailymov/>) at 04:25 UT. The centroid of the extended source region, as determined from the pre-eruption filament location, was at N50°; the source Carrington longitude was $\sim 85^\circ$. The filament extended over the west limb as seen from STEREO B, making this nearly a limb CME for STEREO B. Figure 1 shows the evolution of the CME eruption using four images from STEREO B. The top left image shows the erupting prominence on the NW limb as seen in EUVI 304 Å at 5:16 UT. The top right shows a difference image of the CME at 7:45 UT, and the bottom left (right) shows a difference image of the CME in COR2 B at 13:38 UT (16:38 UT). We note that a gradual deflection from $\sim 85^\circ$ toward the equator is seen throughout both the COR1 ($1.5 R_{\text{sun}} < R < 4.3 R_{\text{sun}}$) and COR2 ($2.5 R_{\text{sun}} < R < 15 R_{\text{sun}}$)

Figure 1 Case 1: Four views from STEREO B on 2008 December 12. Upper left: EUVI 304 Å image at 5:16 UT showing the erupting prominence on the NW limb. Upper right: COR1 difference image of the CME at 07:45 UT. Lower left (right): COR2 difference image of the CME at 13:38 (16:38) UT. A gradual southward deflection from the source at $\sim 50^{\circ}$ N is clearly seen.

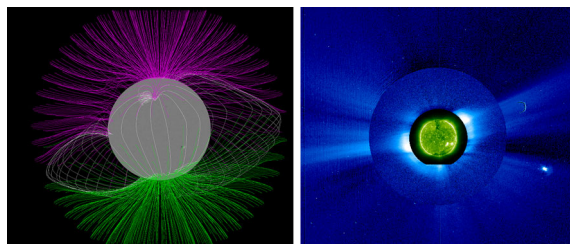
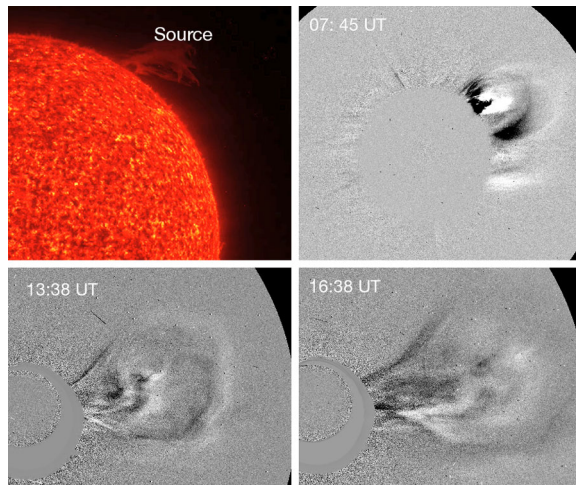


Figure 2 Case 1: Comparison of PFSS model for 2008 December 12 (left) and corresponding pre-event corona (right), both seen from the STEREO A viewpoint. The PFSS model shows the last closed fields line (white) and the CME prominence arcade (white) as well as open field lines (magenta and green). The location of the streamers as seen in white light corresponds to the location of the PFSS model HCS (at cusps of the last closed field lines).

fields of view. Such a gradual deflection is typical behavior for polar crown filament eruptions moving under the influence of the large-scale coronal magnetic fields. The latitude (longitude) of the CME as it left the COR2 FOV, determined from STEREO A and B coronagraph images and the fitting procedure described in Section 2, was $N8^{\circ}$ (74); this agrees very well with the trajectory given by Gui *et al.* (2011), who used the same fitting technique. Thus there was a southward deflection in latitude of 42° and an eastern deflection in longitude of 11° (Table 1). The asymmetric southward-dominated expansion, analyzed by Byrne *et al.* (2010), can also be seen in the sequence of SECCHI coronagraph images in Figure 1. Thus the nonradial propagation seems to result from an asymmetric expansion as the CME pushes its way out of the corona.

Figure 2 compares the PFSS model (left) for 2008 December 12 at 0 UT with the pre-event corona (right) for this CME, both from the STEREO A point of view. The coronal image is a composite of EUVI 195 Å, COR1, and COR2 images from approximately the same time (~ 0 UT), created using the Festival software (<http://www.ias.u-psud.fr/stereo/festival/>). The PFSS model shows the last closed field line (white), the CME prominence arcade near disk center from this point of view (white) and the open field lines (magenta and green). We note that the location of the PFSS HCS (at the cusps of the last closed field lines) on

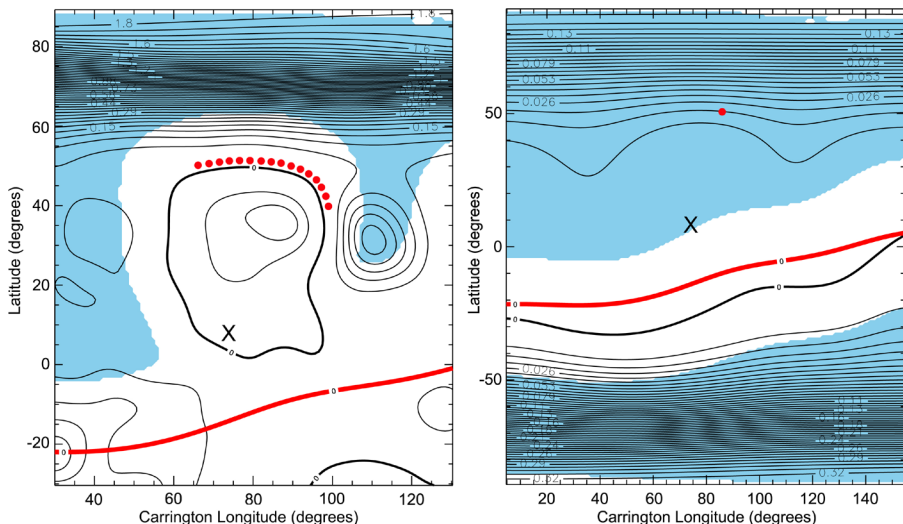
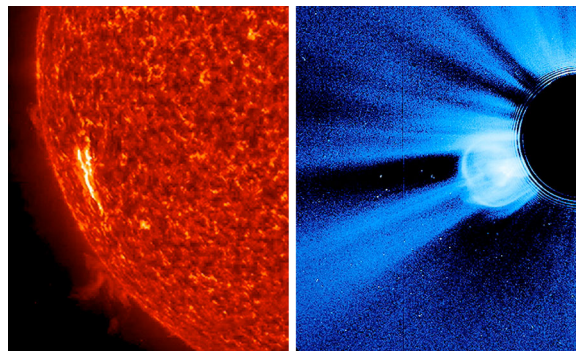


Figure 3 Case 1: Contour plots of B^2 from the PFSS model of 2008 December 12 at 0 UT. The final CME trajectory is marked with an X, the region of open field lines is shaded blue, and the solid red line is the current sheet at $2.5 R_{\text{sun}}$. Left: Contours at $R = 1.2 R_{\text{sun}}$ with the location of the H α filament marking the source region indicated with red dots. The contours show a strong gradient in magnetic pressure to the north of the source, pushing the CME southward, and a weaker gradient pushing eastward. Right: Contours at $1.6 R_{\text{sun}}$ show a gradient guiding the CME toward the weak field region around the HCS. The source location centroid is shown as a red dot.

the east limb agrees with the streamer belt location observed by STEREO A. We interpret the brighter upper streamer belt and fainter lower streamer belt seen on the west limb as a result of the tilt of the HCS at the longitudes of STEREO A's west limb. The brighter belt is at the approximate latitude of a flat portion of the HCS just in front of the limb; the fainter belt is at the approximate latitude of a flat portion of the HCS behind the limb and farther from the plane of sky. This gives us confidence in the large-scale coronal field structure of the PFSS model. Similar comparisons of the PFSS current sheet and the location of the pre-event streamer belt were made for all five cases in this study to give us confidence that the PFSS model was a good representation of the coronal magnetic fields.

Figure 3 shows contours of the magnetic pressure from the PFSS model at two representative heights in the corona, 1.2 (left) and $1.6 R_{\text{sun}}$ (right). The x - y axes here and in all the contour plots are Carrington longitude and heliographic latitude; the region of open field lines at the same height as the contour is shaded blue. The HCS at $2.5 R_{\text{sun}}$ calculated from the model is shown here and in subsequent figures as a solid red line. The angular coordinates of the final CME trajectory are marked with an X. The location of the pre-eruption filament from H α observations is shown here and in subsequent figures as a sequences of red dots at the lower height; a single red dot marks the source centroid in the contour plot on the right. The contours at $1.2 R_{\text{sun}}$ show magnetic pressure gradients that would push the CME southward toward the current sheet and also somewhat eastward, as observed. The magnetic pressure gradient to the west is associated with open flux from an extension of the polar coronal hole as well as with arcade fields and is stronger than the gradient associated with the open flux to the east, leading to the slight eastward component of the deviation. Higher up, at $1.6 R_{\text{sun}}$, (right panel) the gradient in the magnetic pressure continues to guide the CME southward. We conclude that the large-scale coronal magnetic fields have guided

Figure 4 Case 2: Two views of the Sun on 2010 April 3 from STEREO A. Left: An EUVI 304 Å image at 9:56:15 UT showing the source region flare ribbons. Right: The CME as seen in COR2 at 10:24 UT. The CME appears to propagate radially out along a pre-existing streamer.



the CME out through the weak field region surrounding the HCS. This is commonly observed during solar minimum, as discussed in the introduction. We note that the CME does not follow the shortest path to the HCS, but rather follows the direction dictated by the local and global magnetic pressure gradients along the path.

The PFSS model (Figure 2, left) shows that the prominence arcade (white) lies below the open flux from the coronal hole extension (pink) to the east. The field from this coronal hole contributes to the weak gradient east of the source, as discussed above. The curvature of the field lines in PFSS model suggests that the tension of the open field lines might also contribute to the observed eastward deflection of 11° .

3.2. Case 2: CME on 2010 April 3

The fast ($> 800 \text{ km s}^{-1}$) CME on 2010 April 3 was associated with an active-region filament eruption in AR 11059 starting at approximately 9 UT. Various other aspects of this CME have been extensively discussed by others (Wood *et al.*, 2011; Xie *et al.*, 2012; Rouillard *et al.*, 2011). Liu *et al.* (2011) studied the many remote-sensing and *in situ* observations of this CME and used a triangulation technique on the STEREO coronagraph and heliospheric imager data to study the propagation in the ecliptic to 1 AU. The source region (latitude = $S25^\circ$, longitude = 261°) was very accurately determined from STEREO A/EUVI 195 and 304 Å images of the flare ribbons seen shortly after 9 UT and also from the PEA seen starting around 10 UT. Figure 4 shows two views of the Sun from STEREO A: An EUVI 304 Å image at 9:56:15 UT showing the source region flare ribbons (left) and the CME as seen in COR2 at 10:24 UT (right). Difference images of the CME can be found in Figure 6 of Liu *et al.* (2011); these show a rather symmetric expansion of the CME. In this case the CME does not appear to be deflected, but rather appears to propagate radially from the source. This was confirmed by the GCS determination of the trajectory (latitude = $S25^\circ$, longitude = 259°). It also appears to propagate in the direction of a pre-existing streamer, visible in Figure 4, and also in the pre-event coronal image (not shown). The location of the pre-event streamer, as seen in Figure 4 and in the pre-event corona, agreed well with the location of the PFSS model HCS, giving us confidence that the model describes the corona well in the vicinity of the CME.

Figure 5 shows contour plots of magnetic pressure from the PFSS model of 2010 April 3 at 6 UT at two representative heights in the corona, $R = 1.1 R_{\text{sun}}$ (left) and $R = 1.6 R_{\text{sun}}$ (right). As in Figure 3, the HCS from the model at $2.5 R_{\text{sun}}$ is shown as a solid red line, the source location (filament) as red dot(s), the CME trajectory as an X, and the open field line region at the same height as the contours is shaded blue. In this case, the source and

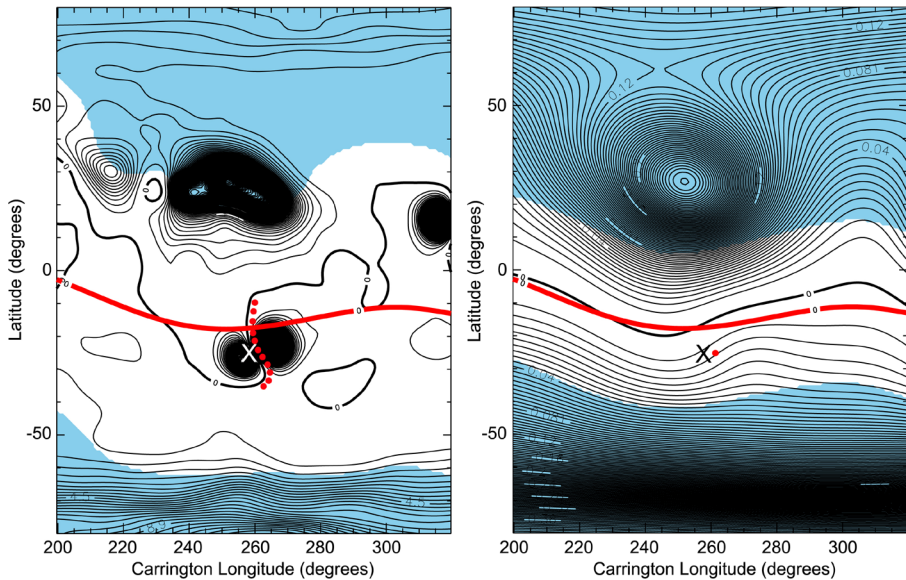


Figure 5 Case 2: Contour plots of B^2 from PFSS model of 2010 April 3 at 6 UT, labeled as in Figure 1. Left: Contours at $1.1 R_{\text{sun}}$, show that the source region lies in a local maximum of magnetic pressure directly below the current sheet. Right: Contours at $1.6 R_{\text{sun}}$ show that source region (red dot) and trajectory (X) lie in the broad minimum of the magnetic field energy density field minimum around the current sheet.

the trajectory are at the same location, indicating no measurable deviation in either latitude or longitude. Moreover, they both lie nearly on the HCS. The left contour plot at $1.1 R_{\text{sun}}$, shows the source region located within a local maximum in magnetic pressure, so there is no gradient to deflect the CME away from the source region. The contour plots on the right show that the source and trajectory are within the broad weak field and weak gradient region around the current sheet. In this case, the CME therefore moves out radially and leaves the corona in the vicinity of the HCS, which here is 25° south of the solar equator.

3.3. Case 3: CME on 2010 April 8

The moderate velocity ($V \sim 500 \text{ km s}^{-1}$) CME on 2010 April 8 originated in AR 11060 at approximately 2:30 UT; the initial stages of the eruption and the accompanying EIT wave were investigated in detail by Liu *et al.* (2010c) using images from the SDO *Atmospheric Imaging Assembly* (AIA) and STEREO. Colaninno, Vourlidas, and Wu (2013) determined the trajectory, but did not address the nonradial propagation. The source region can be well determined from either the SDO or STEREO observations. The source region latitude is $N24^\circ$ and the trajectory latitude, as determined by the GCS fitting to the STEREO A and B coronagraph images, was $S7^\circ$, giving a southward deviation from the source of 31° . In this case, the apparent deflection results from the very asymmetric expansion of the CME very low in the corona. The Carrington longitude of the source (trajectory) was 180° (195°), giving a westward deviation of 15° .

Figure 6 shows three views of the corona as seen from STEREO A; the images are composites of EUVI, COR1 and COR2 images as in Figure 2. The left image shows the pre-event corona at 0 UT. The center image shows the CME in the COR1 FOV at 4:00 UT. In the COR1 difference movie, the CME is seen to be propagating near the solar equator even

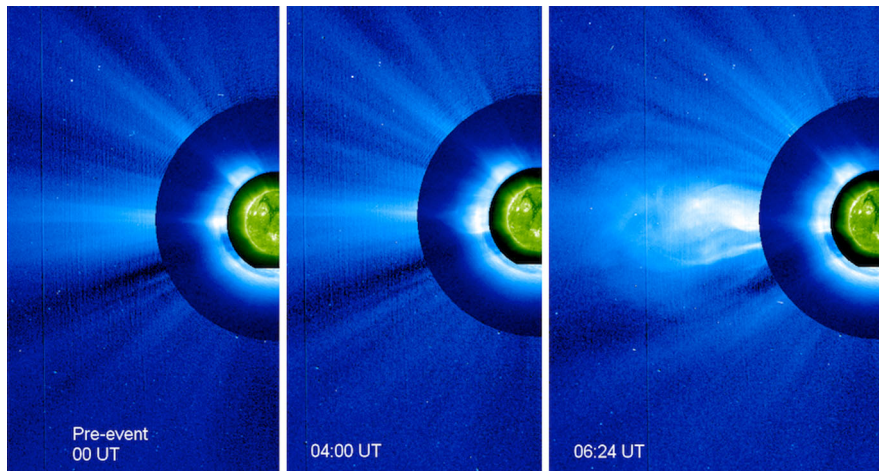


Figure 6 Case 3: Three composite views of the corona from STEREO A on 2010 April 8. Left: Pre-event corona at 0 UT. Center: The CME, seen in the COR1 FOV at 4 UT, is shown to propagate near the equator; the source was at N25. Right: The CME, seen in the COR2 FOV at 6:24 UT. The CME is already propagating near the equator in the COR1A FOV at 04:00 UT and appears to propagate out along the pre-existing streamer shown on the east limb in the pre-event corona.

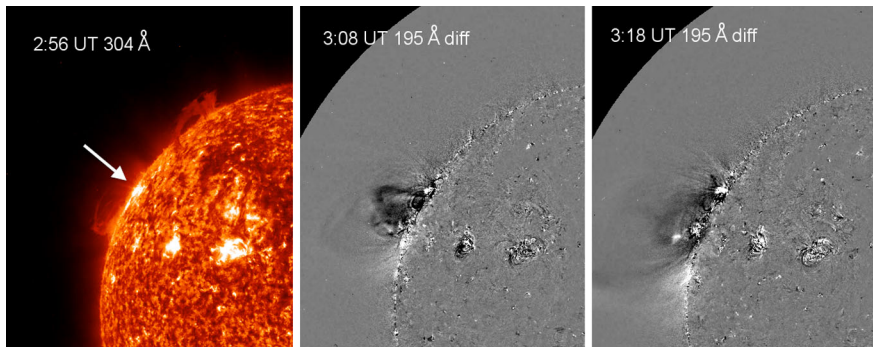


Figure 7 Case 3: Three images from the STEREO A point of view on 2010 April 8. Left: EUVI 304 Å image early in the eruption showing the location of the source at N25° (white arrow). Center (Right): EUVI 195 Å difference image at 3:08 (3:18) UT showing that the CME expands asymmetrically to the south from the source region within the EUVI FOV.

as it enters the COR1 FOV at about 3:30 UT. Thus the deviation from the source latitude N25° to the solar equator has occurred low in the corona – inside 1.5 R_{sun}. The image on the right shows the CME in the COR2 FOV at 6:24 UT. The CME appears to propagate out in the direction of the pre-existing streamer, seen on the east limb in the pre-event corona.

Figure 7 shows three views from STEREO A illustrating the rapid asymmetric southward expansion of this CME within the EUVI FOV. The image on the left shows the source region (white arrow) in EUVI 304 Å at 2:56 UT. The center (right) image shows an EUVI 195 Å difference image at 3:08 (3:18) UT showing that the CME expands only southward from the source. EUVI 195 Å images also show that the dimming region also only extends southward. The asymmetric expansion of both the CME and the EUV wave can also be seen

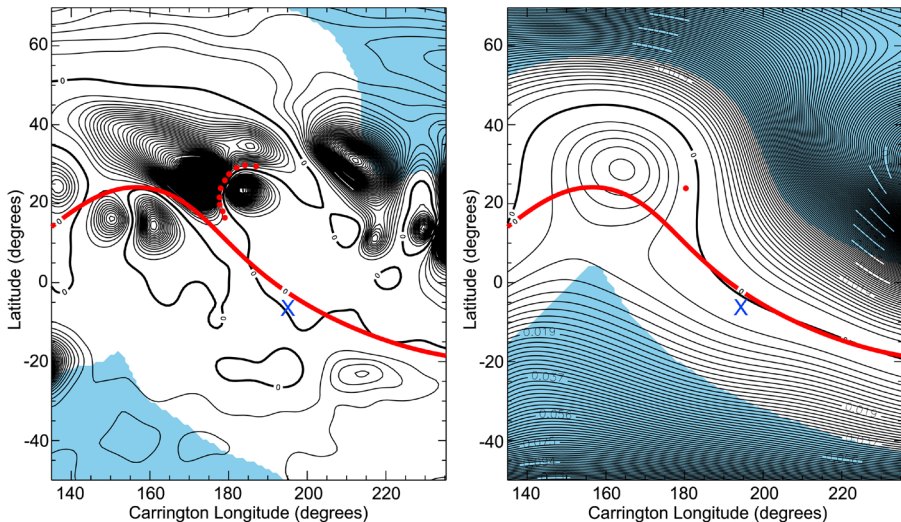


Figure 8 Case 3: Contour plots of B^2 from PFSS model of 2010 April 8 at 0 UT, labeled as in Figure 1. Left: Contours at $1.1 R_{\text{sun}}$, showing that the source region lies on a steep gradient of magnetic pressure that causes the CME to expand asymmetrically to the southwest. Right: Contours at $1.6 R_{\text{sun}}$. The magnetic pressure gradient appears to guide the CME along the current sheet and the trajectory (X) passes through the region of minimum magnetic field energy density around the HCS.

in Liu *et al.* (2010c) (see their Figure 1 and accompanying video material); they found that the propagating EUV disturbance was strongest in the southwest and attributed the asymmetric expansion to strong active-region fields to the north, consistent with our analysis. For this case, the deviation from the source region therefore occurs near the surface, within the EUVI FOV ($R < 1.5 R_{\text{sun}}$).

Figure 8 shows contour plots of the magnetic pressure from the PFSS model for 2010 April 8 at 0 UT at two heights in the corona, $R = 1.1 R_{\text{sun}}$ (left) and $R = 1.6 R_{\text{sun}}$ (right); the current sheet (solid red line), source (red dot; filament-red dots), and trajectory (X) are labeled as in previous contour figures; the regions of open field lines at that height are shaded blue. The plot shows at $R = 1.1 R_{\text{sun}}$ that the source region (in AR 11060) lies on a very steep pressure gradient in the magnetic field near the solar surface due to the strong active-region fields mainly to the northeast. This strong pressure gradient pushes the CME in the southwest direction and explains the asymmetric expansion near the solar surface, seen in projection in Figure 7. Thus here the active-region fields play a major role in causing the deviation from radial propagation. Higher up in the corona, as seen in the $R = 1.6 R_{\text{sun}}$ contour plots in Figure 8, the gradients act to guide the CME along the HCS. The CME deviation from the source, 31° southward and 15° westward, follows the tilt of the current sheet. Thus this CME is also seen to exit the corona in the weak field, weak magnetic gradient region around the current sheet. The CME propagates near the equator because the inclined HCS crosses the equator at the longitude of the CME. As in Case 1, the CME does not follow the shortest route to the HCS, but takes a path dictated by the local and global magnetic pressure gradients.

3.4. Case 4: CME on 2010 May 1

The slow ($< 300 \text{ km s}^{-1}$) CME on 2010 May 1 is associated with a filament eruption that began late on April 30. The nonradial motion of the erupting prominence, but not the CME, has

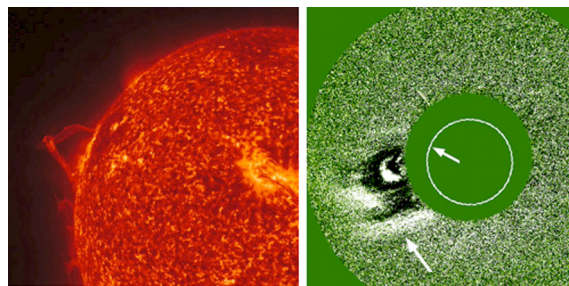


Figure 9 Case 4: Two views of the 2010 May 1 CME as seen from STEREO A. Left: EUV 304 Å image on April 30 at 23:46:14 UT showing the erupting filament near the east limb; the filament centroid was at approximately N20°. Right: COR 1 difference image on May 1 at \sim 1:30 UT showing the CME propagating near the solar equator; the source region is indicated by the upper white arrow. A southward steamer deflection is shown in the difference image (lower white arrow).

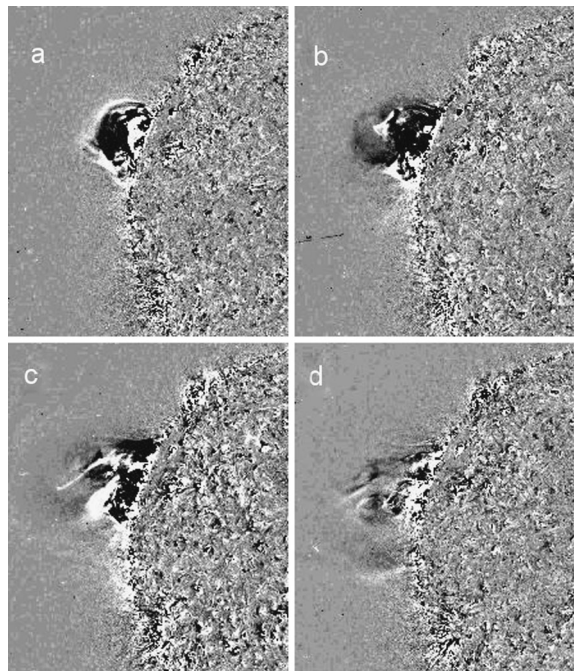
been analyzed by Panasenco *et al.* (2013) using observations and a PFSS model; it is noted in this article that the magnetic configuration creates the conditions for nonradial propagation of the corresponding CME. The location of the source region, as determined from the location of the pre-eruption filament in H α , was N20° and the Carrington longitude 233°, west of the small active region AR 11064 and east of AR 11063. The trajectory longitude (latitude), as determined by the GCS fitting to the STEREO A and B coronagraph images, was 207° (S8°), giving a deviation from radial propagation of -26° (-28°) in longitude (latitude).

Figure 9 shows two views of the event from STEREO A. The EUVI 304 Å image (left) shows the erupting filament April 30 at 23:46:14 UT. The right image shows a COR1 difference image at approximately 1:30 UT. At this time, the CME is midway through the COR1A FOV and is well south of the source latitude N20°. The difference image is extracted from the COR1 difference movie (available from <http://cor1.gsfc.nasa.gov/dailymov/>), which shows the nonradial CME propagation southward from the source latitude (upper white arrow). An obvious southward coronal streamer deflection (lower white arrow) can be seen in the difference image in Figure 9: In the difference image, the streamer's former location shows as black and the deflected location as white. Apparently, the CME interaction with the coronal magnetic fields as it pushes out leads to the downward deflection of the streamer. Such interactions of CMEs with the coronal magnetic fields, as evidenced by the streamer deflections and disruptions, are common (Subramanian *et al.*, 1999).

Figure 10 shows a sequence of STEREO A EUVI 195 Å running-difference images showing that the deviation from radial propagations occurs within the EUVI FOV. Image times are (a) 23:35 and (b) 23:50 UT on April 30, and (c) 0:05 and (d) 0:25 UT on May 1. The CME expands asymmetrically downward, causing the streamer deflection seen in the COR1A difference image in Figure 9 (right). Only the southward component of the deviation can be seen in the images in Figure 10. The corresponding downward nonradial motion of the filament itself can be seen in Figure 9 of Panasenco *et al.* (2013).

Analysis of the PFSS model for this event (2010 May 1 at 0 UT) indicates that the CME source region filament channel lies between a compact active region to the SE (AR 11064) and a strong diffuse magnetic field region to the NW (see also Figure 10 of Panasenco *et al.*, 2013). This configuration is shown in the left panel of Figure 11, which shows magnetic pressure contours at 1.05 R_{sun}. We note the steep pressure gradient associated with the compact active region to the SE, as well as the gradients to the NW. Slightly higher, at 1.1 R_{sun} (middle panel), the gradients from the large diffuse magnetic region in the NW dominate

Figure 10 Case 4: Sequence of four STEREO A EUV 195 Å running-difference images showing the asymmetric expansion to the south within the EUVI FOV. Image times are (a) 23:35 and (b) 23:50 UT on 2010 April 30, and (c) 0:05 and (d) 0:25 UT on 2010 May 1.



those of the compact active region and push the CME to the SE, consistent with the southward expansion seen in Figure 9. Comparing the final trajectory location (X) with the source, it appears that the CME passed directly over the compact AR 11064; this was also true of the filament, as is shown in the supplementary video in Panasenco *et al.* (2013). The magnetic pressure gradients at $1.6 R_{\text{sun}}$ (Figure 11, right panel) acts to push the CME to the SE toward the current sheet (solid red line). As in the other cases, the CME exits the corona in the weak field region around the HCS, but does not reach it by taking the shortest path. Since the steamer belt generally coincides with the HCS, the streamer deflection, shown in Figure 9, is also evidence that the CME is exiting near the HCS.

Using the same PFSS model, the competition between the magnetic pressures of the compact active region and the strong diffuse region is illustrated in Figure 12. The left panel shows the variation in the magnetic pressure gradients with height for a fixed slice in latitude at 20° , passing through the center of the filament. The red arrow indicates the filament longitude at this latitude. The CME may in fact be accelerated by the combined influence of these competing magnetic forces through the “melon seed” effect (Pneuman, 1984). The structure of the coronal magnetic field lines at the filament center longitude ($232^\circ - 233^\circ$) is shown in the right panel of Figure 12. The closed white field lines of the filament arcade lies below the canopy of open field lines. The CME trajectory presumably follows near the boundary between the open and closed field lines, deflecting the streamer belt as it propagates out.

3.5. Case 5: CME on 2010 August 14

The fast ($> 800 \text{ km s}^{-1}$) CME on 2010 August 14 is associated with a filament eruption from AR 11093 at approximately 9:30 UT. The filament eruption and radio emissions associated with this CME have been studied in detail by Tun and Vourlidas (2013), but the

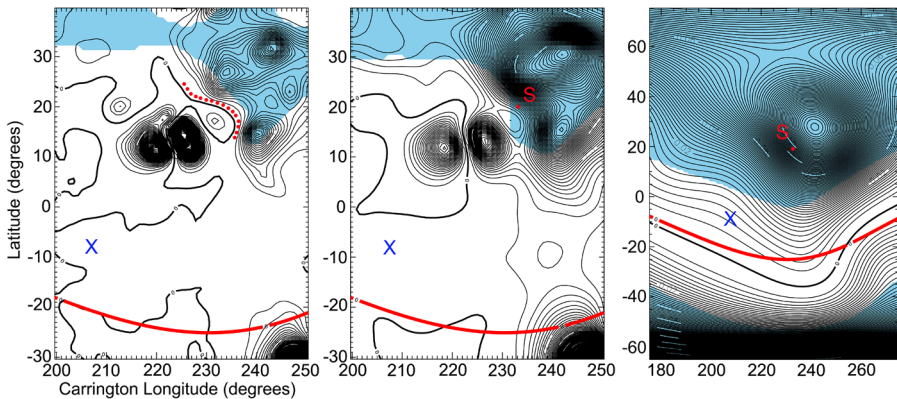


Figure 11 Case 4: B^2 contours from PFSS model of 1 May at 0 UT at three heights, increasing left to right, labeled as previous contour plots. At $1.05 R_{\text{sun}}$ (left), the steepest gradient is that of the compact active region to the SE of the source region, marked by the filament, whereas at $1.1 R_{\text{sun}}$ (center) the steep gradient from the magnetic fields in the NW dominates, pushing the CME to the SE. The trajectory takes the CME up and over the compact active region. The B^2 contours at $1.6 R_{\text{sun}}$ (right) show that the magnetic pressure is pushing the CME from source (S) to a final trajectory (X) in the weak field region around the heliospheric current sheet.

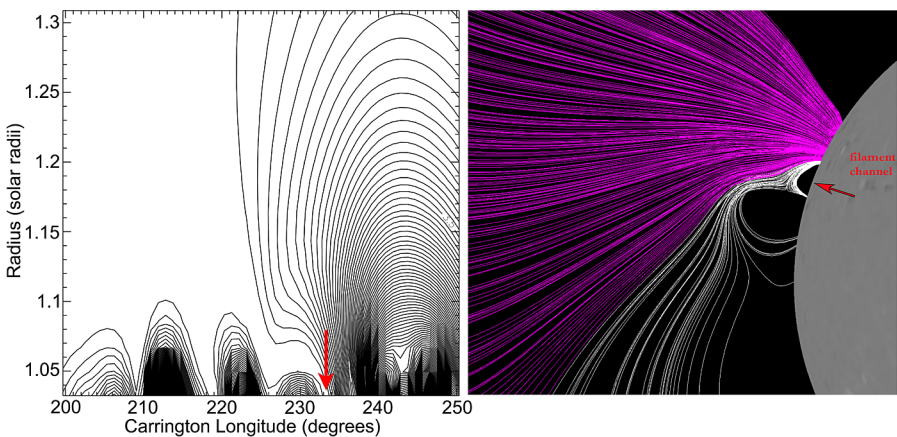


Figure 12 Case 4: Left: Contours of B^2 plotted as a function of height for a fixed slice in latitude at 20° passing through the center of the filament on 1 May 2010 at 0 UT, illustrating the variation in magnetic pressure with height. At very low heights, strong magnetic pressure gradients are shown on both sides of the filament channel, which may have additionally accelerated the CME as it is squeezed out between them. Right: A slice of the PFSS model field lines at $232 - 233^\circ$ longitude, showing the white closed field lines of the filament arcade and the closed field lines of the compact active region to the SE (see text).

nonradial CME propagation was not analyzed. The location of the source region, as determined from the location of the pre-eruption filament in H α , was N13° and the Carrington longitude 351°. Figure 13 shows composite images of the corona from STEREO A, showing the EUVI 195 Å, COR1, and COR2 images. The image on the left shows the pre-event corona at approximately 0 UT; the extended AR source region is indicated by the white arrow. The image on the right shows the CME in the COR2 FOV at approximately 11 UT; note the shoulder on the northern edge of the CME. The CME is propagating well south of

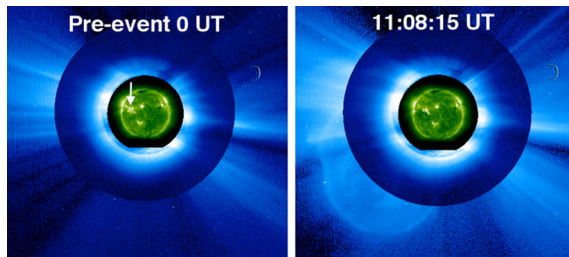
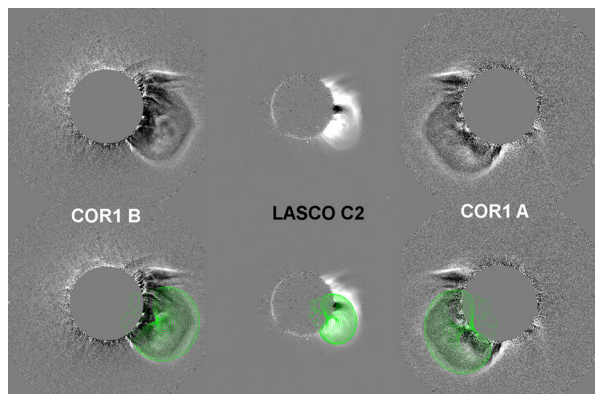


Figure 13 Case 5: Two views of the corona from STEREO A on 2010 August 14. Left: The pre-event corona at 0 UT. The extended source region (AR 11903) is indicated by the white arrow. Right: CME in COR2 FOV at 11:08:15 UT, showing propagation well south of the source region. Note the delayed front of the CME at the northern edge.

Figure 14 Case 5: GCS fitting of the 2010 August 14 CME at 10:35 UT. Top row, left to right: difference images from COR1 B, LASCO C2, and COR1 A. The COR1 images show streamer deflections to the north and south caused by the CME and/or its shock. Bottom: The GCS model (green) fit to the three views shown in the top row. Note the good match of the model all along the bright CME leading edge.



the source latitude and does not appear to propagate in the direction of a pre-event streamer. The trajectory as determined by the GCS fitting was S13° and Carrington longitude 341°, giving a southward (eastward) deviation of 25° (13°).

A more detailed investigation revealed that the CME front observed in COR2 had been considerably distorted on the northern side by interaction with the surrounding corona within the COR1 FOV. For this case, both COR1 and COR2 observations and three viewpoints were used in the fitting – STEREO A and B and LASCO. Figure 14 shows the GCS fitting of the CME in the COR1 and LASCO/C2 FOVs, all at 10:35 UT. The top row shows the difference images from the three points of view; the bottom row shows the GCS fit (green) to the images. Two important features are revealed by these images. First, the CME front is well rounded and is fit by the leading edge of the flux rope along its entire length. Second, streamer deflections are evident just to the south and also to the north of the CME. These are evidence of the CME and its shock interacting with the streamer belt as the CME exits the corona.

The GCS fitting at a later time in Figure 15 shows the dramatic results of the interaction with the streamer belt. The upper row shows difference images from the STEREO and SOHO points of view, but now farther out, in the STEREO COR2 and LASCO/C3 FOVs. We note that the CME front has changed shape significantly and is no longer well rounded; the front is distorted at the northern end, presumably due to interactions with the streamer belt. The bottom row shows the fit to the self-similar expansion of the CME fit in the COR1 FOV, *i.e.*, the GCS model was moved out radially from the positions determined in the COR1

Figure 15 Case 5: GCS fitting of the 2010 August 14 CME at approximately 11:24 UT. Top row, left to right: difference images from COR2 B, LASCO C2, and COR2 A. The distortion of the CME front in the north is evident. Bottom: Same views as the top row, now with the model (green). The interaction with the streamer has delayed the northern end of the CME front; the delay is indicated by white arrows.

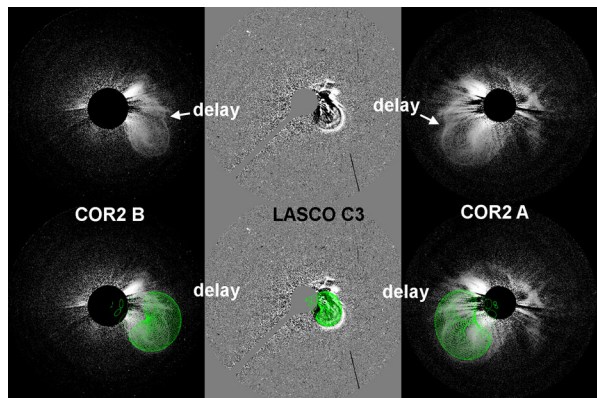
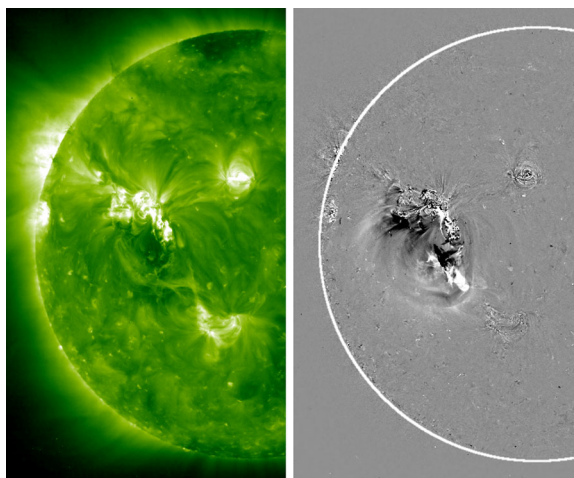


Figure 16 Case 5: EUVI 195 Å images from STEREO A. Left: direct image at 9:50 UT. Right: Difference image at 9:50 UT showing that the dimming only spreads southward from the AR 11903 complex, indicating an asymmetric expansion of the CME. Note the bright active region to the north of the dimming region in the left image.



and C2 images, such as Figure 14, and the dimension scaled with the distance from the Sun. As a result of the distortion in the front, the observed CME front does not match the leading edge of the GCS model for the entire length; the northern end of the CME front has been delayed by its interaction with the streamer. This is a clear case of the large-scale coronal fields affecting the CME trajectory and the CME affecting the large-scale structure of the corona. The front seen in the COR2 image in Figure 12 (right panel) also clearly shows this distortion. This distortion makes it appear as if the CME is propagating even farther south than the S13° determined from the fitting shown in Figures 14 and 15.

The deviation from the source at N13° to propagation at S13°, determined from the COR1 fits, occurs very low in the corona. For this eruption, as for Case 3, a rapid asymmetric expansion of the CME leads to an apparent deflection from the source within the EUVI FOV. Figure 16 shows direct (left) and difference (right) EUVI 195 Å images at 9:50 UT during the eruption. The difference image shows that the expansion is asymmetric and only southward. The direct image shows a very bright active region lying just to the northwest. Both the filament and the CME can be seen to head southward in the supplemental online movies, with 304 Å showing the filament and 195 Å showing that the dimming region spreads only southward. This suggests that asymmetric dimming regions and EUV wave fronts are signatures of the nonradial propagation of the associated CME.

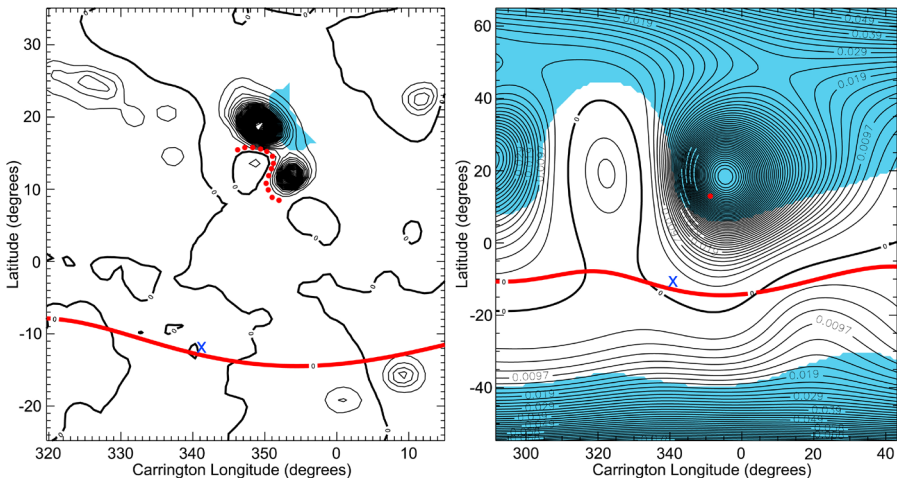


Figure 17 Case 5: Contours of B^2 from PFSS model of 2010 August 14 at 6 UT. Left: Contours at $1.03 R_{\text{sun}}$, showing that the source region lies just south of a very strong field region that causes the observed southward asymmetric expansion. Right: B^2 contours at $1.6 R_{\text{sun}}$ show that the magnetic pressure has pushed the trajectory (T) south such that the CME exits the corona in the weak field region around the HCS. Plot labeling is explained in the caption to Figure 1.

Figure 17 shows the contour of the magnetic pressure for the PFSS model for this day at 6 UT for two heights in the corona; the left (right) plot shows the contours at 1.03 ($1.6 R_{\text{sun}}$); labels are as in previous contour plots. The contour plot at $1.03 R_{\text{sun}}$ shows that the source region filament (red dots) lies south and east of very steep magnetic field gradients associated with the bright active region seen in Figure 16 (left). The strong magnetic fields of this active region act as walls on the CME expansion, forcing the asymmetric expansion mainly southward, but also eastward. The contour plot at $1.6 R_{\text{sun}}$ in Figure 17 shows the trajectory (T) in relation to the PFSS CS (solid red line), indicating that again the CME continues to be pushed mainly southward and that it exits the corona through the weak field region around HCS. Although the images in Figure 13 suggest that the CME propagates out below the streamer belt, the contour plot at $1.6 R_{\text{sun}}$ and the fact that a streamer was pushed out of the way indicate that the CME is leaving the corona near the streamer belt and HCS.

4. Summary and Discussion

We have investigated the role of the coronal magnetic fields in the nonradial propagation of CMEs near the Sun ($< 15 R_{\text{sun}}$) by analyzing the 3D trajectories of five CMEs for which the solar source regions and 3D trajectories are well determined. The trajectories (heliographic latitude, Carrington longitude, velocity) were determined by fitting multi-viewpoint coronagraph observations using the GCS forward-modeling technique (Thernisien, Howard, and Vourlidas, 2006). The deviation from radial propagation is, then, the difference between the source angles and the trajectory angles. A PFSS model was used to estimate (1) the local and global magnetic pressure on the CME at various heights in the corona and (2) the location of the HCS. For all cases, we compared the location of the HCS with that of the streamer belt in the vicinity of the CME to gain confidence in the PFSS model. We ascertained whether or not the CMEs exited the corona near the weak field region surrounding the HCS as determined from the PFSS.

We find that for two of the CMEs (Cases 3 and 5) a large ($\geq 25^\circ$) deviation in latitude of the trajectory from the source results from a rapid initial asymmetric expansion within the EUVI FOV ($R < 1.5 R_{\text{sun}}$); the asymmetric expansion is caused by the magnetic pressure of active region fields in the immediate vicinity of the eruption. One of these (Case 5) was the fastest CME analyzed ($V = 867 \text{ km s}^{-1}$, *cf.* Table 1) and demonstrates that even fast CMEs can be deflected by the coronal fields. We conclude that large local active-region magnetic fields as well as the overlying global coronal magnetic fields are important in determining the trajectories of CMEs. For both of these cases, the CMEs are subsequently guided out of the corona through the weak field region around the HCS.

In one case with a very large deviation in latitude and longitude (Case 4), we find that while the trajectory is influenced close to the surface by a nearby small compact active region, above about $1.1 R_{\text{sun}}$ the magnetic pressure forces are dominated by a stronger diffuse magnetic region pushing in the opposite direction. This results in an asymmetric expansion observed within the EUVI FOV and a nonradial trajectory. The magnetic pressure gradient from the stronger diffuse region pushes the CME toward the weak field region around the HCS, apparently passing directly above the nearby compact active region. In another case (Case 2), a fast CME lies at the top of a local minimum in the magnetic pressure that lies directly below the HCS; this CME propagates radially outward from the source with no deviation in latitude and insignificant deviation in longitude. Yet another case (Case 1) follows a familiar scenario in periods of low solar activity: a CME associated with a polar crown filament eruption is gradually deflected toward the region of the HCS by the large-scale magnetic fields. We find that in all five cases, within the approximations inherent in using the PFSS to determine the HCS, the CMEs exit the corona in the weak field region surrounding the HCS, even when the HCS is highly tilted and warped. This agrees with the results and conclusions of Shen *et al.* (2011) and Gui *et al.* (2011).

The streamer belt and the HCS are generally co-located. CMEs interacting with the coronal magnetic fields often cause streamer deflections as they propagate out through the coronagraph FOVs (Subramanian *et al.*, 1999; Lugaz *et al.*, 2009). If CMEs have more kinetic plus magnetic pressure than that of the coronal streamer and if CME is propagating out through the streamer belt, such deflections are to be expected. Such interactions will also affect the evolution of the CME. In one case (Case 5) we saw how such an interaction distorted the shape of the CME front without causing a change in the trajectory as such.

The fact that all the CMEs in studies such as ours and that of Gui *et al.* (2011) exit through the HCS is closely related to the fact that the coronal streamers associated with the closed field source regions coincide with the HCS. Wang (2015) has recently noted that CMEs associated with pseudostreamers form a separate class of CMEs. It may be that such CMEs do not exit the corona near the HCS since pseudostreamers do not coincide with the HCS streamer belt. This is currently under investigation (Panasenco, 2015).

Even if most CMEs exit the corona in the vicinity of the HCS and streamer belt, it will be difficult to predict the trajectory of a fast CME during periods of solar activity because (1) the HCS can be quite warped and the CME can be deflected in both latitude and longitude and (2) there are many CME–CME interactions. We find, however, that the gradients in the magnetic pressure very near the surface – those associated with closed field regions – should also be considered in any attempt to predict the CME final trajectory. Moreover, our results indicate that other observable signatures of asymmetric CME expansion and nonradial propagation are a coronal dimming region and/or initial EUV wave front that spread preferentially in one direction from the source. Thus if an asymmetric dimming region and/or bright EUV wave front are observed at the start of the eruption, the CME will mostly likely not propagate radially from the source location.

CME–CME interactions in and beyond the corona can clearly change CME trajectories, either through a merging of the CMEs (Lugaz and Roussev, 2011; Lugaz *et al.*, 2012) or deflection, as described by Lugaz *et al.* (2012) and Shen *et al.* (2012). It is questionable whether the actual trajectory of a major CME can be altered by interaction with the solar wind since the CME momentum flux is significantly higher than that of the surrounding solar wind, roughly by the square of the ratio of the velocities. However, interaction of the CME with the solar wind has been observed in data (Savani *et al.*, 2010; Liu *et al.*, 2009) and simulations (Manchester *et al.*, 2004; Lugaz *et al.*, 2009) to distort the shape of the CME front, and this may be misinterpreted as a deflection in analyzing the coronal and heliospheric images. As shown in our Case 5, distortion can occur even within the COR2 FOV. Distorted portions of the CME propagating into slower, denser solar wind and moving slower than portions propagating into less dense, faster wind are expected and observed. Distortion in shape will also effect CME arrival times. These various effects mean that an accurate prediction of whether and when a fast CME will impact Earth will probably require solar and heliospheric imaging from multiple viewpoints.

Acknowledgements We would like to thank R.A. Howard, N. Sheeley, M. Velli and V. Pizzo for useful discussions on various aspects of this research. We also thank the referee for very useful comments that have improved the article. The work of PCL was conducted at the Jet Propulsion Laboratory, California Institute of Technology under a contract from NASA. The work of OP was supported by a subcontract from the Jet Propulsion Laboratory. The work of AV and RC was supported by NASA contract S-136361-Y to the Naval Research Laboratory. AV is also supported by internal JHU/APL funds. The STEREO/SECCHI data used here are produced by an international consortium of the Naval Research Laboratory (USA), Lockheed Martin Solar and Astrophysics Lab (USA), NASA Goddard Space Flight Center (USA) Rutherford Appleton Laboratory (UK), University of Birmingham (UK), Max-Planck-Institut für Sonnensystemforschung (Germany), Centre Spatial de Liège (Belgium), Institut d’Optique Théorique et Appliquée (France), Institut d’Astrophysique Spatiale (France).

References

- Byrne, J., Maloney, S.A., McAteer, J., Refojo, J.M., Gallagher, P.T.: 2010, *Nat. Commun.* **1**, 74. [DOI](#).
- Colaninno, R., Vourlidas, A., Wu, C.C.: 2013, *J. Geophys. Res.* **118**, 6866. [DOI](#).
- Cremades, H., Bothmer, V.: 2004, *Astron. Astrophys.* **422**, 307.
- Cremades, H., Bothmer, V., Tripathi, D.: 2006, *Adv. Space Res.* **38**, 461.
- DeForest, C.E., Howard, T.A., McComas, D.J.: 2013, *Astrophys. J.* **769**, 43. [DOI](#).
- Gopalswamy, N., Mäkelä, P., Xie, H., Akiyama, S., Yashiro, S.: 2009, *J. Geophys. Res.* **114**, A00A22.
- Gui, B., Shen, C., Wang, Y., Ye, P., Liu, J., Wang, S., Zhao, X.: 2011, *Solar Phys.* **271**, 111. [DOI](#).
- Howard, R.A., Sheeley, N.R. Jr., Koomen, M.J., Michels, D.J.: 1985, *J. Geophys. Res.* **90**, 8173.
- Howard, R.A., Moses, J.D., Vourlidas, A., Newmark, J.S., Socker, D.G., Plunkett, S.P., Korendyke, C.M., Cook, J.W., Hurley, A., Davila, J.M., *et al.*: 2008, *Space Sci. Rev.* **136**, 67.
- Hundhausen, A.J.: 1993, *J. Geophys. Res.* **98**, 13177.
- Kay, C., Opher, M., Evans, R.M.: 2013, *Astrophys. J.* **775**, 5. [DOI](#).
- Kilpuua, E.K.J., Pomoell, J., Vourlidas, A., Vainio, R., Luhmann, J., Li, Y., *et al.*: 2009, *Ann. Geophys.* **27**, 4491.
- Liewer, P.C., Hall, J.R., De Jong, E.M., Socker, D.G., Howard, R.A., Crane, P.C., Reiser, P., Rich, N., Vourlidas, A.: 2001, *J. Geophys. Res.* **106**, 15903.
- Liu, Y., Luhmann, J.G., Lin, R.P., Bale, S.D., Vourlidas, A., Petrie, G.J.D.: 2009, *Astrophys. J. Lett.* **698**, L51.
- Liu, Y., Davies, J.A., Luhmann, J.G., Vourlidas, A., Bale, S.D., Lin, R.P.: 2010a, *Astrophys. J. Lett.* **710**, L82.
- Liu, Y., Thernisien, A., Luhmann, J.G., Vourlidas, A., Davies, J.A., Lin, R.P., Bale, S.D.: 2010b, *Astrophys. J.* **722**, 1762.
- Liu, W., Nitta, N.V., Schrijver, C.J., Title, A.M., Tarbell, T.D.: 2010c, *Astrophys. J.* **723**, L53.
- Liu, Y., Luhmann, J.G., Bale, S., Lin, R.P.: 2011, *Astrophys. J.* **734**, 84. [DOI](#).
- Lugaz, N., Roussev, I.I.: 2011, *J. Atmos. Solar-Terr. Phys.* **73**, 1187. [DOI](#).
- Lugaz, N., Vourlidas, A., Roussev, I.I., Morgan, H.: 2009, *Solar Phys.* **256**, 269. [DOI](#).
- Lugaz, N., Farrugia, C.J., Davies, J.A., Möstl, C., Davis, C.J., Roussev, I.I., Temmer, M.: 2012, *Astrophys. J.* **759**, 68. [DOI](#).

- MacQueen, R.M., Hundhausen, A.J., Conover, C.W.: 1986, *J. Geophys. Res.* **91**, 31.
- Manchester, W.B., Gombosi, T.I., Roussev, I., Ridley, A., De Zeeuw, D.L., Sokolov, I.V., Powell, K.G., Tóth, G.: 2004, *J. Geophys. Res.* **109**, 2107.
- Möstl, C., Amla, K., Hall, J.R., Liewer, P.C., De Jong, E.M., Colaninno, R.C., et al.: 2014, *Astrophys. J.* **787**, 119. [DOI](#).
- Odstrcil, D.: 2004, *J. Geophys. Res.* **109**, A02116. [DOI](#).
- Panasenco, O., 2015, Private communication.
- Panasenco, O., Martin, S., Joshi, A.D., Srivastava, N.: 2011, *J. Atmos. Solar-Terr. Phys.* **73**, 1129.
- Panasenco, O., Martin, S., Velli, M., Vourlidas, A.: 2013, *Solar Phys.* **287**, 391.
- Plunkett, S.P., Thompson, B.J., St. Cyr, O.C., Howard, R.A.: 2001, *J. Atmos. Solar-Terr. Phys.* **63**, 389. [DOI](#).
- Pneuman, G.W.: 1984, *Solar Phys.* **94**, 387.
- Rouillard, A.P., Odstrcil, D., Sheeley, N.R., Tylka, A., Vourlidas, A., Mason, G., et al.: 2011, *Astrophys. J.* **735**, 7. [DOI](#).
- Savani, N.P., Owens, M.J., Rouillard, A.P., Forsyth, R.J., Davies, J.A.: 2010, *Astrophys. J. Lett.* **714**, L128. [DOI](#).
- Schrijver, C.J., DeRosa, M.L.: 2003, *Solar Phys.* **212**, 165.
- Schwenn, R.: 2000, *Adv. Space Res.* **26**, 43.
- Shen, C., Wang, Y., Gui, B., Ye, P., Wang, S.: 2011, *Solar Phys.* **269**, 389.
- Shen, C., Wang, Y., Wang, S., Liu, T., Liu, R., Vourlidas, A., Miao, B., Ye, P., Liu, J., Zhou, Z.: 2012, *Nat. Phys.* **8**, 923. [DOI](#).
- Subramanian, P., Dere, K.P., Rich, N.B., Howard, R.A.: 1999, *J. Geophys. Res.* **104**, 22321.
- Thernisien, A.: 2011, *Astrophys. J. Suppl.* **194**, 33.
- Thernisien, A.F.R., Howard, R.A., Vourlidas, A.: 2006, *Astrophys. J.* **652**, 763. [DOI](#).
- Thernisien, A.F.R., Vourlidas, A., Howard, R.A.: 2009, *Solar Phys.* **256**, 111.
- Tun, S., Vourlidas, A.: 2013, *Astrophys. J.* **766**, 130.
- Wang, Y.-M.: 2015, *Astrophys. J.* **805**, L12. [DOI](#).
- Wang, Y.-M., Sheeley, N.R., Rich, N.B.: 2000, *J. Geophys. Res.* **27**, 149.
- Wood, B.E., Wu, C.-C., Howard, R.A., Socker, D.G., Rouillard, A.P.: 2011, *Astrophys. J.* **729**, 70.
- Xie, H., Odstrcil, D., Mays, L., St. Cyr, O.C., Gopalswamy, N., Cremades, H.: 2012, *J. Geophys. Res.* **117**, A04105. [DOI](#).
- Zhou, Y.F., Feng, X.S.: 2013, *J. Geophys. Res.* **118**, 6007. [DOI](#).
- Zuccarello, F.P., Bemporad, A., Jacobs, C., Mierla, M., Poedts, S., Zuccarello, F.: 2012, *Astrophys. J.* **744**, 66. [DOI](#).